Journal of Materials Science & Technology 204 (2025) 190–203

Contents lists available at ScienceDirect

Journal of Materials Science & Technology

journal homepage: www.elsevier.com/locate/jmst

Research Article

A facile high-efficiency preparation strategy for Al-containing multi-component boride microcrystals with superior comprehensive performance

Yong Fan[a], Jinfeng Nie[a,*], Zhigang Ding[a], Yujing Zhang[b], Xiang Chen[a], Wei Liu[a], Sen Yang[b], Sida Liu[c,*], Xiangfa Liu[d], Yonghao Zhao[a,e,*]

[a] Nano and Heterogeneous Materials Center, School of Materials Science and Engineering, Nanjing University of Science and Technology, Nanjing 210094, China
[b] School of Materials Science and Engineering, Nanjing University of Science and Technology, Nanjing 210094, China
[c] Laboratory for multiscale mechanics and medical science, SV LAB, School of Aerospace, Xi'an Jiaotong University, Xi'an 710049, China
[d] Key Laboratory for Liquid–Solid Structural Evolution and Processing of Materials, Ministry of Education, Shandong University, Jinan 250061, China
[e] School of Materials Science and Engineering, Hohai University, Changzhou 213200, China

ARTICLE INFO

Article history:
Received 12 November 2023
Revised 7 February 2024
Accepted 17 February 2024
Available online 10 April 2024

Key words:
Multi-component borides
First-principles calculations
Crystal growth
Mechanical properties
Oxidation behavior

ABSTRACT

Multi-component transition group metal borides (MMB_2) have become a research hotspot due to their new composition design concepts and superior properties compared with conventional ceramics. Most of the current methods, however, are complicated and time-consuming, the mass production remains a challenge. Herein, we proposed a new high-efficiency strategy for synthesis of MMB_2 using molten aluminum as the medium for the first time. The prepared Al-containing multi-component borides $(TiZrHfNbTa)B_2$ microcrystals had a homogeneous composition with a hexagonal AlB_2 structure and ultra-high hardness value of ~35.3 GPa, which was much higher than data reported in the literature and the rule of mixture estimations. Furthermore, combined with the First-principles calculation results, we found that the Poisson's ratio (v) values exhibit a clearly ascending trend from 0.17 at VEC = 3.5 to 0.18 at VEC = 3.4, then to 0.201 at VEC = 3.2 with the increasing of Al content. This indicates that the intrinsic toughness of multi-component boride microcrystals is obviously enhanced by the trace-doped Al elements. Besides, the fabricated Al-containing multi-component boride microcrystals have superior oxidation activation energy and structural stability. The enhanced oxidation resistance is mainly attributed to the formation of a protective Al_2O_3 oxide layer and the lattice distortion, both of which lead to sluggish diffusion of O_2. These findings propose a new unexplored avenue for the fabrication of MMB_2 materials with superior comprehensive performance including ultra-hardness and intrinsically improved thermo-mechanical properties.

1. Introduction

Conventional transition metal borides (TMBs), such as TaB_2, ZrB_2, TiB_2, are being widely studied over the past few decades due to their excellent mechanical properties, corrosion resistance, high-temperature stability and catalytic characteristics [1–3]. These borides belong to the ultra-high-temperature ceramics (UHTCs) family, and are expected to have wide applications in extreme environments, such as aerospace, solar energy, nuclear reactors, metallurgy, cutting tools, and microelectronics [4,5]. However, due to the constraints of compositional space, the performance space of these single-phase TMBs is limited. Besides, their inherent brittleness and poor high-temperature oxidation resistance significantly limit their development and wide application. With an increasing demand for higher performance, the design of UHTCs with desirable properties at certain service conditions has become an urgent issue to be addressed in the academic community.

Nowadays, the concept of multi-component solid solutions (also namely medium- or high-entropy) modification of UHTCs materials candidates brings new opportunities for the further improvement of the comprehensive properties [6–8]. Recently, the multi-component transition group metal borides (MMB_2) have gained

---

* Corresponding authors..
E-mail addresses: niejinfeng@njust.edu.cn (J. Nie), sidaliu@xjtu.edu.cn (S. Liu), yhzhao@njust.edu.cn (Y. Zhao).

https://doi.org/10.1016/j.jmst.2024.02.074
1005-0302/

increasing attention due to their higher hardness, increased high temperature phase stability and better oxidation resistance than single-phase TMB_2 [9–12]. For instance, Demirskyi et al. reported that $(Zr_{1/2}Ta_{1/3}Nb_{1/6})B_2$ exhibited excellent specific strength at 1600 °C due to the ongoing plastic deformation [11]. Chu et al. fabricated $(Hf_{0.28}Zr_{0.28}Ta_{0.28}W_{0.15})B_2$, which displayed superior oxidation resistance at a wide temperature range of 1473–1773 K in air [13]. It is illustrated that the MMB_2s will exhibit superior mechanical and interesting physical properties due to the mass disorder and solution hardening with different valence electrons and atomic radii in the crystal structure [14,15].

Up to now, a variety of solid-state reaction methods have been proposed for the synthesis of MMB_2 including high energy ball milling, spark plasma sintering (SPS) and boro/carbothermal reduction method, etc. [9,16-19]. Although the obtained products have high composition uniformity, the solid-state reaction method also exhibited some disadvantages, such as complex preparation process, high energy consumption and long preparation cycle, which are not conducive to the rapid design and wide application. Several novel attempts, such as sol-gel method and molten salt synthesis, have been reported for the preparation of MMB_2 [20,21]. Although these methods have the advantages of low reaction temperature and nanoscale powder size, the problems of expensive metal powders and toxic inorganic reaction have not been solved. Therefore, it is still needed to develop a low-cost, energy-saving and high-efficient synthesis approach for MMB_2.

Generally, the high hardness of MMB_2 is always accompanied with high brittleness remains a big challenge, which severely limits their practical application. This is due to the fact that currently prepared MMB_2 are usually composed of IVB and VB refractory transition metal borides, such as ZrB_2, TiB_2, etc., which are proved to be more brittle [22]. Recent studies have demonstrated that increasing the configurational entropy, manipulating valence electron concentration (VEC), and doping some other ductile elements like Al will be an effective strategy for toughening materials [14,23-25]. Therefore, employment of a multi-component concept by varying the metal constituent in the design of ceramics with enhanced toughness is of great interest to the UHTC community.

In addition, developing MMB_2 with superior oxidation resistance is also urgent to achieve their potential applications as ultrahigh-temperature structural materials. Unfortunately, most of the previous studies mainly focus on exploiting the mechanical and thermal properties of MMB_2, while its oxidation resistance is ignored. To the best of our knowledge, few research effort has been devoted to the oxidation resistance of MMB_2. Gild et al. [9] observed that MMB_2 have better oxidation resistance compared to the rule of mixtures and each boride precursor. The authors attributed the enhanced anti-oxidation resistance of these MMB_2 to the large compositional design space which is propitious to form better protective oxide scales. Backman [26,27] pointed out that preferential oxidation occurred according to the difference in relative thermodynamic stability of the constituent oxides and formed a protective layer of complex oxides on the surface of the MMB_2s phase during the oxidation process.

Although the large compositional design space of MMB_2 tends to facilitate the formation of better protective scales, the oxidation resistance of the MMB_2 remains unsatisfactory [28]. This is due to the fact that previously reported studies mainly focused on the isothermal oxidation behavior of the MMB_2 [11,13,29], where the authors proposed the oxidation pathway of MMB_2, but the detailed kinetic analysis was not revealed. In general, thermal oxidation essentially involves non-isothermal heating, and the kinetics will help define how the material should be used in practical applications. Therefore, understanding the kinetics of non-isothermal oxidation is crucially important to design a material with superior oxidation resistance. However, few studies on the non-isothermal stability of MMB_2 are available at present. Furthermore, materials that are designed for a specific application consider the size and thermal stability, and the understanding of reaction kinetics occurred during the thermal process is also necessary. In a nutshell, revealing the non-isothermal oxidation kinetics of the MMB_2s phase is essential.

In this work, we proposed a new and highly efficient method to synthesize MMB_2 particles in a molten aluminum medium using the spontaneous in-situ reaction between dissolved transitional metal atoms and boron atoms. It is demonstrated that solid solution hardening was the primary reason for the superior hardness of MMB_2. Furthermore, it is proved that doping Al into MMB_2 is a promising strategy to produce ceramic particles with inherently improved toughness and oxidation resistance. A particular and controllable approach was provided for the design and synthesis of MMB_2 particles with improved comprehensive performance. This work will serve a new perspective on the microstructure modulation of MMB_2, which can enhance our understanding of the distinctive properties of MMB_2 and promote the exploration of new properties and applications.

2. Experimental method

2.1. Sample preparation

The detailed fabrication process of the $(HfNbTaTiZr)B_2$ particles in the aluminum matrix is shown in Fig. 1. The raw materials utilized in the present experiment are pure Ti (99.90 wt%), pure Zr (99.50 wt%), Hf (99.95 wt%), Nb (99.95 wt%), Ta (99.95wt%), Al (99.99 wt%) and Al-B master alloy. Melting of the samples was done in an argon arc furnace with a water-chilled copper crucible. The nominal composition of the prepared aluminum alloy containing the boride particles is shown in Table 1. The as-cast ingots were fabricated on a water-cooled copper crucible using vacuum arc melting by WK-II (Beijing Physcience Opto-electronics Co., Ltd, China) under argon environment. The raw materials are placed in ascending order of their melting points in the water-cooled copper crucible. During the melting process, the arc discharge was maintained for 90–120 s with the power source current of 200 A. In order to minimize microstructural heterogeneity, the alloys were flipped and re-melted for five times. For comparison, single phase TiB_2, ZrB_2, NbB_2, TaB_2 and HfB_2 were also synthesized in the aluminum, respectively. Afterward, a 20 wt% hydrochloric acid was used to prepare the corrosive liquid to dissolve the matrix Al in the arc-melting products and the extracted particles were gathered for the further observed.

2.2. Microstructure characterization

The microstructure of bulk alloy was analyzed by field emission scanning electron microscope (FESEM, Quanta250F) equipped with Oxford energy dispersive X-ray spectrometer (EDS). The phase structure of the extracted powder was studied by X-ray diffraction (XRD, Bruker-AXS D8). The morphology and crystal structure were observed by FESEM and transmission electron microscope (TEM, Tecnai20, FEI). The nanoscale characterization was conducted using high-resolution transmission electron microscope (Titan G2 60-300). Atom probe tomography (APT, LEAP 4000X SI, Cameca Instruments) was used to analyze the element distributions in the MMB_2 particle. The measurements were performed in voltage mode at 50 K, and the pulse repetition rate is 200 kHz. Samples for APT analyses were prepared with the tips perpendicular using a dual-beam focused ion beam (Zeiss Auriga).

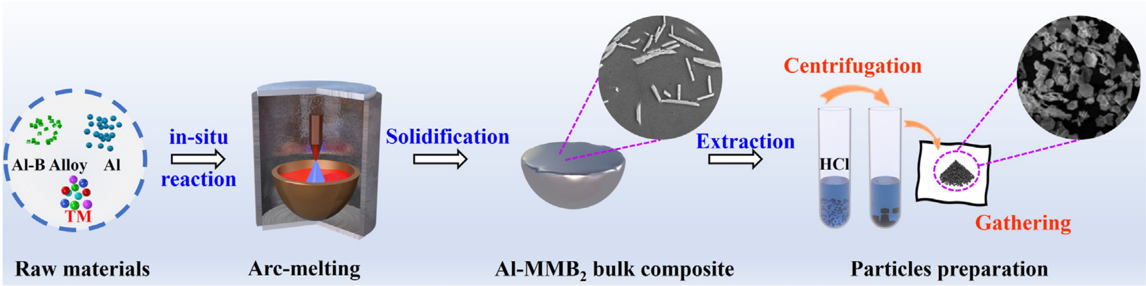

Fig. 1. The fabrication process of the Al-MMB$_2$ bulk composites and MMB$_2$ particles.

Table 1
List of designed combinations used to synthesize the Al-MMB$_2$ bulk alloy (molar fraction).

Hf	Ta	Zr	Nb	Ti	B	Al
0.5	0.5	0.5	0.5	0.5	5	Bal.

2.3. Hardness measurements

In order to determine the mechanical properties of MMB$_2$ particles formed in aluminum alloy and compare them with the single phase transition metal boride, the nano-indentation test was carried out using the Brook haistron Technology Hysitron TI1980 nano-indenter. Indentation test was conducted to a load of 1500 µN and the holding time was set at 2 s to reduce the effect of soft aluminum matrix on the properties of MMB$_2$ particles and avoid its brittle fracture. Both the loading and unloading time was 5 s. At least five indents were conducted on the borides for each sample to achieve statistically meaningful measurements.

2.4. Oxidation test

The non-isothermal oxidation test of the MMB$_2$ powders was examined using Thermogravimetric Analysis-Differential Scanning Calorimetry (TG–DSC; STA 499 f3, Netzsch, Germany). The heating process was carried out from room temperature to 1300 °C in dry air at a heating rate of 5, 10 and 20 °C/min, and the rate of air flow was kept constant at 50 ml/min during heating. SEM and XRD were used to observe and analyze the microstructure and morphology of the oxidized powders.

2.5. First-principle calculation

A supercell (3 × 3 × 3) with 81 atoms is used to simulate the $(Hf_{0.2}Nb_{0.2}Ta_{0.2}Ti_{0.2}Zr_{0.2})B_2$ solid solution crystal structures. The Hf, Nb, Ta, Ti and Zr atoms are located at 1a (0, 0, 0) and boron atoms occupy 2d (1/3, 2/3, 1/2) Wyckoff positions (see Fig. S1). In order to study the effect of Al doping on the mechanical properties of MMB$_2$, 4 and 12 Al atoms were used to replace the transition metal atoms in the MMB$_2$ supercell, which were named MMB$_2$–1 and MMB$_2$–2 respectively. All density functional theory (DFT) calculations were performed with the projector augmented, wave (PAW) method [30], as implemented in the Vienna Ab-initio Simulation Package (VASP) code [31]. The cut-off energy for the plane-wave basis set was taken as 400 eV. The exchange-correlation function was described by the generalized gradient approximation (GGA) of Perdew-Burke-Ernzerhof (PBE) [32,33]. During VASP calculations, a Monkhorst-Pack k-point mesh of 4 × 4 × 4 was applied to all 81-atom models. The convergence criterion is set as follows: the total energy difference was less than 10^{-5} eV/atom, the Hellmann-Feynman force on each atom was less than 10^{-3} eV/Å and the maximum stress on the atom was within 0.02 GPa. For the AlB$_2$-type crystal structure, there are five independent elastic constants, namely C_{11}, C_{12}, C_{13}, C_{33} and C_{44}. These elastic constants are acquired by energy-strain method, and calculation details are described in ref [34,35]. The elastic modulus and shear modulus were calculated using the Voigt-Reuss-Hill approximation [36]. The Pugh's ratio G/B and Poisson's ratio were utilized to assess the brittleness or ductility of MMB$_2$ compounds. Hardness was evaluated using a widely adopted model, which gives $H = 0.92(G/B)^{1.137}G^{0.708}$, where G and B are the shear and bulk modulus [37]. The Young's modulus E of MMB$_2$ is obtained using the formula $E = 9BG/(3B+G)$, where B and G are the bulk and shear modulus, respectively. The Poisson's ratio (v) was calculated by the following formulation: $v = (3B/2\ G)/2(3B+G)$ [38].

3. Results and discussion

3.1. Morphology and crystal structure characterization of MMB$_2$

As shown in Fig. 2(a), generally MMB$_2$ exhibits a layered hexagonal crystal structure (AlB$_2$-type structure, space group P6/mmm). The layered AlB$_2$ structure consisted of alternating distributed rigid 2D boron nets, with quasi-2D layers of transition metal (TM) cations, on which the metal atoms were randomly located. Fig. 2(b) shows that the MMB$_2$ particle with a size of 5–10 µm in length and 2–3 µm in width were successfully synthesized in the Al matrix. Under higher magnification (Fig. 2(c)), these MMB$_2$ particles showed a plate-like morphology. Fig. 2(c1) presents the corresponding EDS mapping analysis, which indicated that the constituted transition metal elements Hf, Ta, Zr, Nb, and Ti were homogenously distributed in MMB$_2$ on a micrometer scale. The XRD diffraction patterns of the crystals extracted from the Al matrix are shown in Fig. S2, which indicates that only single-phase MMB$_2$ with a hexagonal crystal structure formed in the present condition, without any other phases. Fig. 2(d) shows the typical morphology of the extracted particle when viewed perpendicularly to the plate direction, which exhibited a perfect hexagonal platelet-like morphology and was consistent with the crystal structure shown in Fig. 2(a). The corresponding EDS mapping analysis is presented in Fig. 2(d1), which indicated the homogenous distribution of the Hf, Ta, Zr, Nb, and Ti elements without any elemental segregation or aggregation. Furthermore, we observed that Al elements were also doped into the MMB$_2$ particle and were distributed uniformly. Moreover, two derived morphologies, namely, hexagonal petals and bi-layered hexagonal platelets, were also observed, as shown in Fig. 2(e, f). The TEM images further demonstrated the various morphologies of these particles, as shown in Fig. S3. As indicated in the inset of Fig. S3(a), the exposed surfaces of the hexagonal platelet consisted of low-index {0001} and $\{10\bar{1}0\}$ planes, due

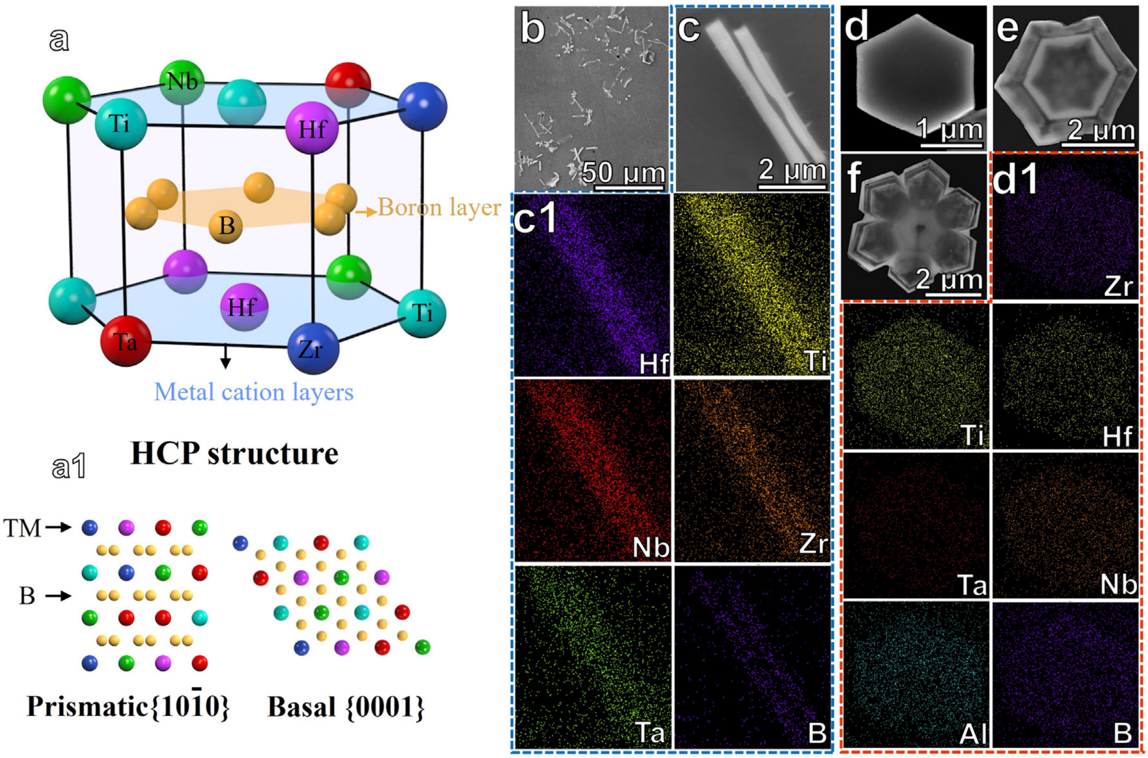

Fig. 2. Synthesis of MMB_2 particles in the aluminum melt. (a) Schematic illustration of the atomic structure and atomic configurations on the corresponding basal {0001} and prismatic $\{01\bar{1}0\}$ planes. The small yellow balls represent boron atoms and the big balls indicate Hf, Ta, Ti, Nb, and Zr. (b, c) SEM images of MMB_2 in the Al matrix. (c1) EDS mapping analysis of particles in (c). (d–f) SEM images showing the three typical crystal morphologies (hexagonal platelet, hexagonal petals, bi-layered hexagonal platelet) of MMB_2. (d1) Elemental distributions in MMB_2 particles in (d).

to their lower surface energy, which agreed well with Fig. 2(a, a1). Therefore, the present $(HfTaZrNbTi)B_2$ particles doped with trace Al elements displayed diverse crystal morphologies, which could be closely related to the different growth mechanisms in the complex melt environment.

The as-synthesized MMB_2 powders were observed by HRTEM along different zone axis as shown in Fig. 3(a) and (b). According to the EDS compositional maps shown in Fig. 3(c), the distribution of Hf, Zr, Ta, Nb and Ti elements was highly uniform at the nanoscale, and no segregation or aggregation was observed among the as-synthesized powders. The atomic configuration along the [0001] zone axis (Fig. 3(a)) is shown in Fig. 3(d). The single crystal exhibited a periodic lattice structure with a set of fringes, with a *d*-space of about 0.275 nm, which corresponded to the $(10\bar{1}0)$ plane of $(HfTaZrNbTi)B_2$. Fig. 3(e) shows the atomic configuration of the (0001) plane at a higher magnification, which clearly revealed that the metal atoms occupied the metal–cation 2D layer of MMB_2, as displayed in Fig. 3(i). Generally, $(HfTaZrNbTi)B_2$ will exhibit a layered hexagonal crystal structure with alternating 2D boron nets and quasi-2D layers of randomly distributed transition metal cations. Due to strong bonding between the B atoms in the B layer and interlayer interactions, the {0001} and $\{10\bar{1}0\}$ planes were quite stable. Furthermore, to observe the atomic configurations on the prismatic plane, the atomic arrangement of MMB_2 was observed along the $[2\bar{1}\bar{1}0]$ zone axis (Fig. 3(b)). Fig. 3(f) directly shows the atomic arrangement on the different (0001) basal planes, which confirmed that the atoms were neatly arranged, and it was consistent with the lattice crystal structure shown in Fig. 3(j).

Furthermore, sever lattice distortions in the MMB_2 crystal structure were determined. Fourier analysis and geometric phase analysis (GPA) were conducted on the high-resolution atomic images to obtain the detailed structure and strain information of the $(10\bar{1}0)$ plane. Fig. 3(g) shows the fast Fourier transform (FFT) reflection pattern of the HRTEM image shown in Fig. 3(d), and the inverse fast Fourier transform (IFFT) images of the purple and red squares in Fig. 3(d), as displayed in Fig. 3(h1, h3). The remarkable distorted fringe patterns in the IFFT image along the $(10\bar{1}0)$ planes indicated that the multiple atoms produced noticeable lattice distortions in MMB_2. The strain distribution in Fig. 3(h1, h3) was also calculated by GPA, and the corresponding strain mapping is shown in Fig. 3(h2, h4), respectively. As presented in Fig. 3(g), the normal directions of the $(\bar{1}2\bar{1}0)$ and $(10\bar{1}0)$ planes were defined as the x-axis and y-axis. The positive and negative strains in GPA mapping were related to the tension and compression regions of distortion. This further demonstrated that nanoscale structural distortions were produced in the prepared MMB_2 particles.

The local chemical analysis of the MMB_2 particles was further analyzed by atom probe tomography (APT), as shown in Fig. 4(a), which indicated that all of the constituent elements in the MMB_2 particles were uniformly distributed on the atomic scale. We also observed that the doped Al elements were uniformly distributed. The one-dimensional concentration-depth profiles of all elements were plotted along a cylindrical region of interest 10 nm in diameter throughout the analyzed volume, as shown in the inset of Fig. 4(b), which revealed no significant concentration fluctuations. The detailed data for each element are shown in Table 2, indicating that the chemical compositions of the as-prepared precipitates were enriched in the Zr element, followed by Hf and Ti elements. However, the Ta ($\sim$1.49 at.%) and Nb ($\sim$1.01 at.%) elements were noticeably depleted in the precipitates. Although Hf, Ta, Zr, Nb and Ti elements were added in an equimolar ratio, the formation of MMB_2 particles occurred through a spontaneous in-situ reaction between the TM atoms and the B atoms at high temperatures. Therefore, the content of each element deviated significantly from the expected normal composition. The content of each metal ele-

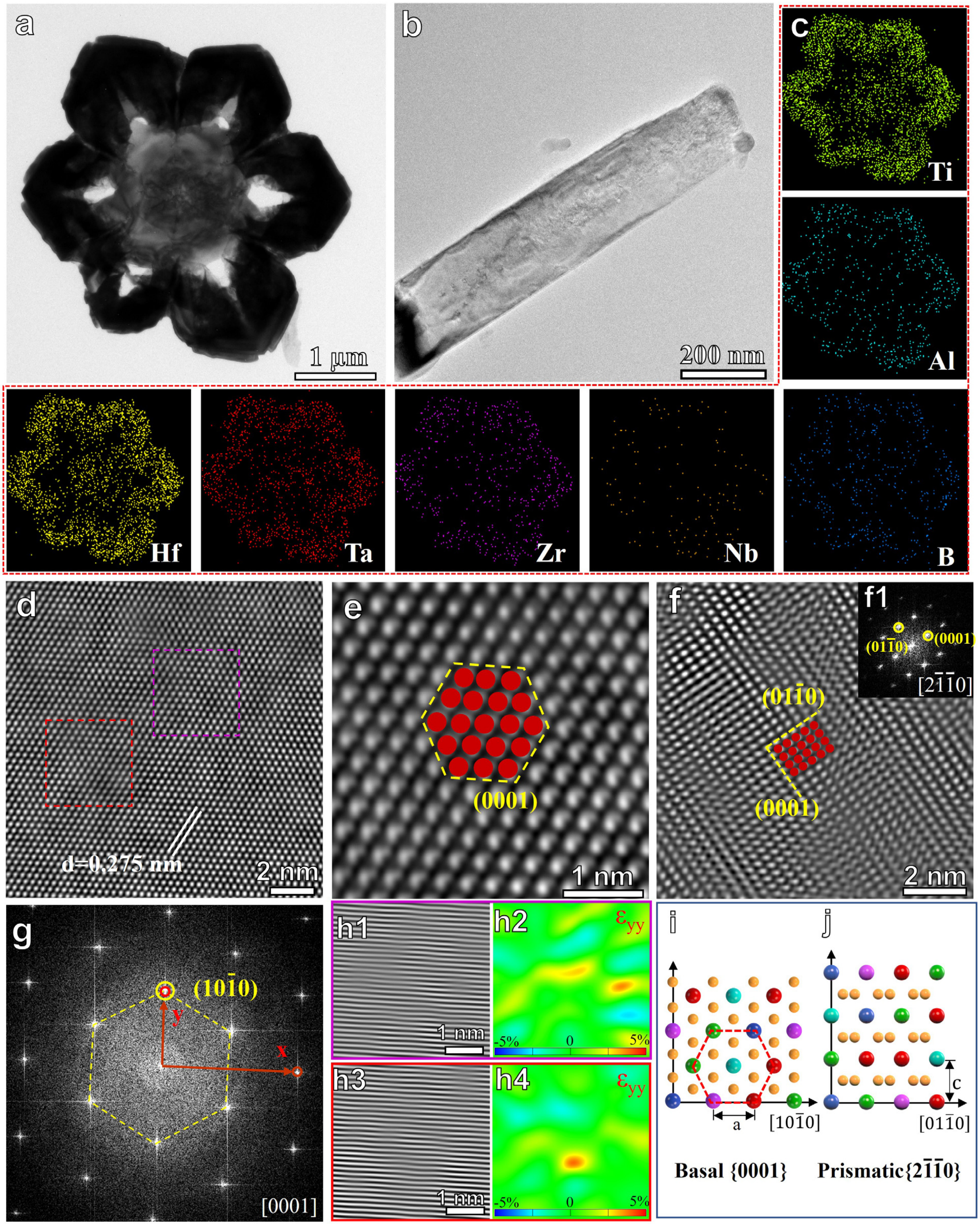

Fig. 3. (a) HRTEM graph of MMB_2 particle, the electron beam is parallel to the [0001] zone. (b) HRTEM graph of another MMB_2 particle, the electron beam is parallel to the [$2\bar{1}\bar{1}0$] zone. (c) The corresponding EDS compositional maps of (a). (d) High-resolution transmission electron microscope (HRTEM) graph of MMB_2 particle and the electron beam is parallel to the [0001] zone, the red and purple squares show the lattice distortion region. (e) HRTEM image at a higher magnification, showing the atomic configuration of (0001) plane. (f) HRTEM graph of another $(HfTaZrNbTi)B_2$ particle alone [$2\bar{1}\bar{1}0$] direction and ($01\bar{1}0$) and (0001) planes are indexed. (f1) the corresponding FFT pattern. (g) FFT pattern of Fig. 2(a). (h1, h3) The IFFT image shows perfect periodicity with noticeable lattice distortion. (h2, h4) GPA mapping showing an overall strain field at nanoscale. The color scale represents change in strain intensity from −5 % (compressive) to 5 % (tensile). (i, j) Schematic illustration of the atomic structure of the MMB_2.

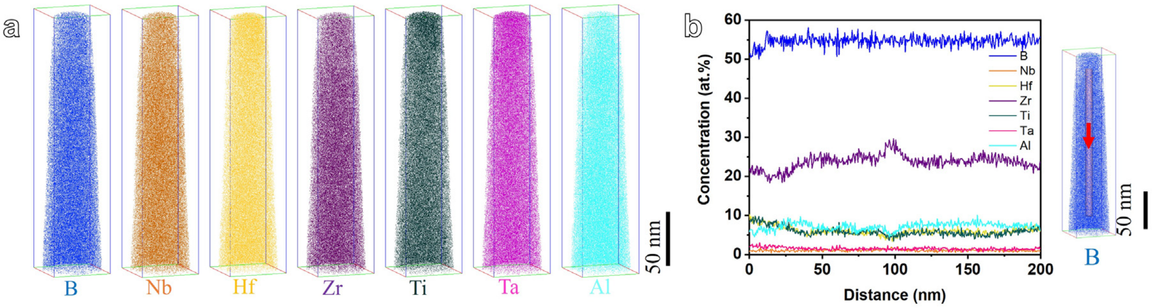

Fig. 4. Local chemical composition analysis of MMB_2 particle by APT. (a) The reconstruction of B, Nb, Hf, Zr, Ti, Ta, and Al atomic positions. (b) The corresponding composition profile from the cylindrical region indicated by the red arrow in the inset.

Table 2
The atomic percentages (at.%) of the MMB_2 particles.

Sample	Zr	Hf	Ti	Ta	Nb	B	Al	O
Experimental	23.449	6.363	6.103	1.490	1.000	54.628	6.960	0.007
Nominal	6.667	6.667	6.667	6.667	6.667	66.667	0	0

ment in the MMB_2 particles was likely influenced by factors such as the size of the TM elements, their ability to combine with B, and their dissolution rate in the aluminum melt. Notably, the prepared MMB_2 contained approximately 6.94 at.% Al elements. This indicates that Al atoms readily incorporated into the crystal nucleation and growth process of MMB_2 in the metallic melt environment.

3.2. Formation mechanism and morphological diversity of $(HfTaZrNbTi)B_2$ microcrystals

According to the above-mentioned crystal morphology analysis, a possible formation process of the MMB_2 in aluminum matrix was proposed with a corresponding schematic diagram, as shown in Fig. 5. As indicated in Fig. 5(a, b), the reaction precursors mainly consisted of pure Ti, Zr, Hf, Nb, Ta, Al-B master alloy, and pure Al in this study. At elevated temperatures, the pure Al would first melt into the liquid phase, while AlB_2 remained solid due to its high melting point. Then, five metals were dissolved into the Al melt and migrated to the liquid-solid interface, reacting with AlB_2, as shown in Fig. 5(c). This could be expressed by Reaction (1):

$$\begin{aligned}&\mathrm{AlB_2}(\mathrm{s})+\frac{1}{5}[\mathrm{Ti}]+\frac{1}{5}[\mathrm{Zr}]+\frac{1}{5}[\mathrm{Hf}]+\frac{1}{5}[\mathrm{Nb}]+\frac{1}{5}[\mathrm{Ta}]\\&\rightarrow(\mathrm{Ti_{0.2}Zr_{0.2}Hf_{0.2}Nb_{0.2}Ta_{0.2}})\mathrm{B_2}(s)+\mathrm{A_l}(\mathrm{l})\end{aligned}\tag{1}$$

where [Ti], [Zr], [Hf], [Nb], and [Ta] represent the dissolved metal atoms in the melt. Once the interface reaction began, the dissolved TM atoms and AlB_2 phase were continuously consumed at the liquid-solid interface, while a concentration gradient formed between the solid and liquid phases, which allowed the reaction to continue.

Arc melting can reach a very high temperature in a short time, allowing it to promote the in-situ reaction due to higher diffusion and reaction rates. The B atoms in the Al-B master alloy dissolved in the Al melt and were subjected to random mixing with the Hf, Ta, Zr, Nb and Ti atoms, as shown in Fig. 5(d). Then multi-component borides with HCP structure could form through the in-situ liquid–solid reaction, according to Reaction (2):

$$\begin{aligned}&\frac{1}{5}[\mathrm{Zr}]+\frac{1}{5}\left[\mathrm{Hf}\right]+\frac{1}{5}\left[\mathrm{Ti}\right]+\frac{1}{5}[\mathrm{Ta}]+\frac{1}{5}\left[\mathrm{Nb}\right]+2[\mathrm{B}]\\&\rightarrow\left(\mathrm{Ti_{0.2}Zr_{0.2}Hf_{0.2}Nb_{0.2}Ta_{0.2}}\right)\mathrm{B_2}(\mathrm{s})\end{aligned}\tag{2}$$

where [B] represents the dissolved boron atoms in the melt. The thermodynamics analysis of the two chemical reactions was calculated, and the detailed results are presented in the Supporting Information. Clearly, the standard Gibbs free energies of Reactions (1) and (2) were negative, and they could proceed spontaneously. With a prolonged reaction time, the concentration of the generated MMB_2 could reach supersaturation. In this case, the MMB_2 would precipitate from the liquid phase and go through the nucleation–growth–morphology transition process.

According to the thermodynamics principle of crystal growth and Wulff's theorem, the equilibrium crystal morphology consisted of the minimum total surface energy, and the faces with lower surface energy would be exposed [39], and close-packed planes with higher reticular densities and large interplane spacing will have lower surface energies. According to crystal structure analysis, MMB_2 consists of three close-packed planes of $\{0001\}$, $\{10\bar{1}0\}$, and $\{10\bar{1}1\}$, which can be preserved as an exposed surface. The order of the surface energy values of these close-packed planes will also impact the equilibrium morphology. For ZrB_2, $\{10\bar{1}0\}$ has the lowest surface energy and will often display rod-like shape under equilibrium conditions. The hexagonal plate-like grain morphology will appear in TiB_2 [40], due to the lowest surface energy of $\{0001\}$. For multi-component transition metal boride, during the liquid-solid reaction process, the doping of different elements will also affect the crystal morphology by changing the surface energy order. For example, Hu et al. [41] successfully synthesized ZrB_2 powders with a flake grain morphology through the addition of Mo, Nb, Ti, W, and Si, which indicated that doping had an important effect on the surface anisotropy of ZrB_2. The equilibrium crystal morphology of MMB_2 in this work had a hexagonal platelet morphology. Significant development of the $\{0001\}$ facets was observed, while the prism was limited by six $\{10\bar{1}0\}$ facets, which was experimentally validated, as shown in Fig. 1(d).

In the subsequent growth process, the morphological diversity of MMB_2 could be determined by the interface-controlled growth. The solid-liquid interface could be divided into two categories: rough and smooth interfaces. Theoretically, the Jackson α-factor can be proposed to predict whether rough or smooth interface-controlled growth models will occur, from the aspect of the material's structure. This could be expressed by the following equation [42]:

$$\alpha=\frac{\Delta H}{RT_{\mathrm{m}}}\left(\frac{\eta}{Z}\right),$$

where ΔH is the enthalpy change, $\frac{\eta}{Z}$ is the fraction of the nearest neighbor sites, consisting of a single layer of molecules on the surface, T_{m} denotes the temperature, and R is the gas constant. For

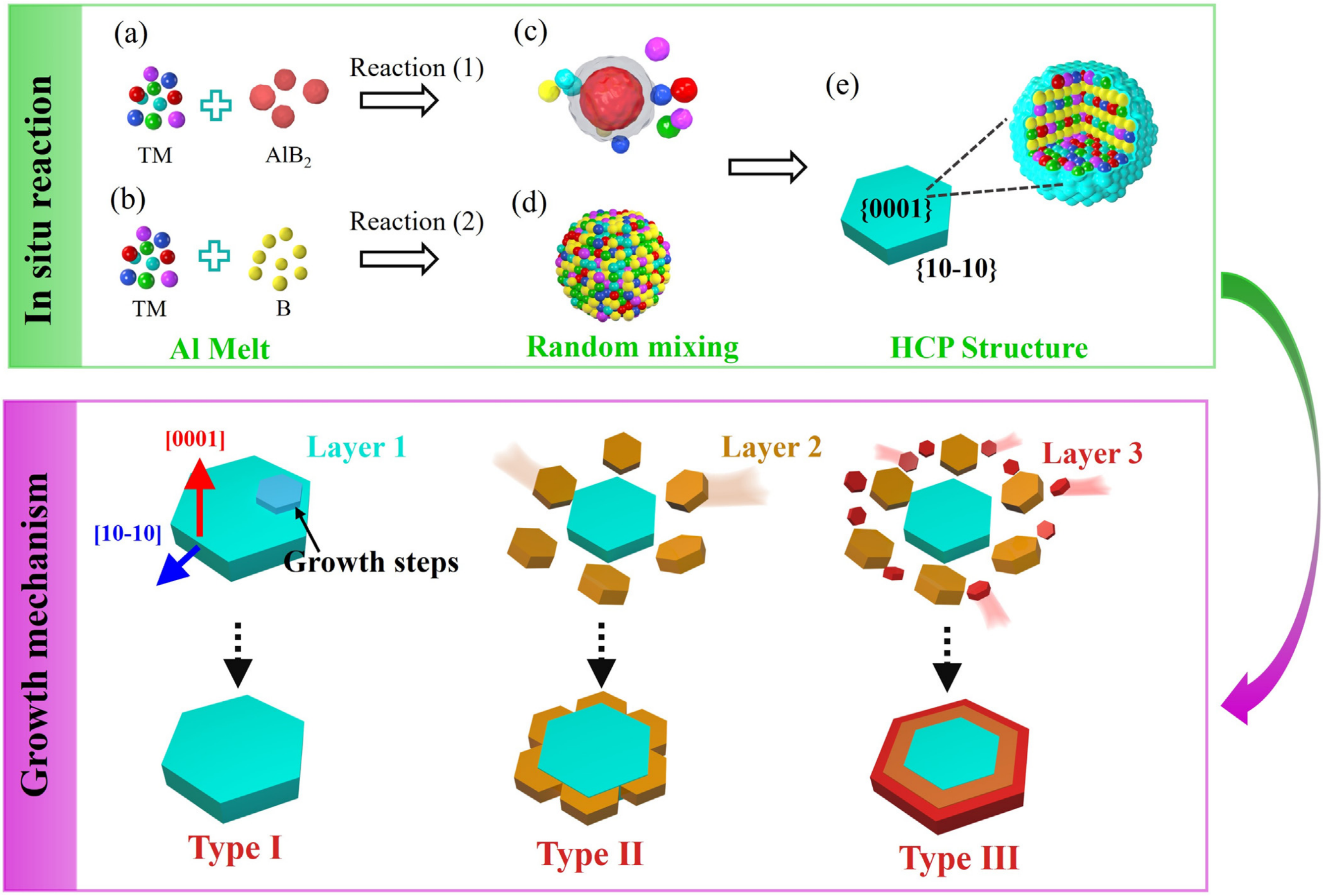

Fig. 5. Schematic illustration of the in-situ reaction and growth mechanism of the MMB_2 microcrystals in the Al melt.

metal borides, the α values of main planes, such as {0001}, {$10\bar{1}0$}, and {$11\bar{2}0$}, were greater than 4 [43], and we inferred that the α values of the planes for high-entropy metal borides were also greater than 4. In this situation, the following growth of the hexagonal platelets was governed by the smooth interface.

The liquid phase growth of crystal smooth interfaces typically includes two-dimensional nucleation growth modes, namely, layer-by-layer growth and screw dislocation-driven growth [44]. Combined SEM and HRTEM analysis of the synthesized products indicated no step and dislocation defects on the synthesized material surface. Therefore, the screw dislocation-driven growth mode could be excluded, and we inferred that MMB_2 grew through two-dimensional nucleation. In addition, due to strong bonding between the B atoms in the B-layer and interlayer interactions, the {0001} and {$10\bar{1}0$} surfaces were quite stable [40]. Thus, the growth mode of the MMB_2 particles in the Al melt consisted of two-dimensional nucleation and smooth surface growth, finally forming a hexagonal plate shape surrounded by the {0001} and {$10\bar{1}0$} planes, as shown in Fig. 5(e).

In the melt environment, the multi-component boride particles had different morphologies, in addition to hexagonal sheet morphology, such as hexagonal petals and bi-layered hexagonal platelets. According to the above analysis, three different types of growth patterns were proposed for MMB_2.

The dissolved TM atoms reacted with the B atoms and thin hexagonal platelets formed firstly in the melt (Type I in Fig. 5). Then, two-dimensional nuclei preferentially appeared on the {0001} facets of the pre-platelets, resulting in the formation of steps. Once a new nucleus originated, it also started to grow in the [0001] and [$10\bar{1}0$] two-dimensional directions. Due to the high temperature and rapid reaction, a large number of primary multi-component boride particles appeared in the melt, and with continued reaction, the concentration of dissolved transition metal and B in the melt decreased, resulting in increased nucleation difficulty. The nucleated multi-component particles were directionally adsorbed on the side of the hexagonal plate, in accordance with a certain symmetry law, which decreased the energy of the system, and was denoted as Type II. Therefore, the unprecipitated metal and B in the melt could quickly accumulate in this step and continue to pile laterally, forming a hexagonal petal-like morphology. However, if the rate of forming steps after adsorption was slow, the subsequent growth units had sufficient time to stack laterally. Finally, the initial side was completely covered, forming a Type III morphology. The diversity of morphology was conducive to the deposition of transition metals, which promoted nucleation and improved the efficiency of particle nucleation.

It was also important to analyze the reaction order of the dissolved transition metal atoms in the Al melt. Table S1 presents the mixing enthalpy (ΔH) of the TM and B atoms, in which the Zr atoms had the lowest mixing enthalpy, followed by Hf, Ti, Ta, and Nb, with the highest mixing enthalpy [45]. Reports have shown that the stiffness and strength of the TM-B bond may decrease following the order of Zr-B (Hf-B), Nb-B, and Ta-B, and the chemical stability of Zr-B is highest compared with Nb-B and Ti-B metal–boron due to enhanced hybridization between TM and B [46,47]. According to the above analysis, it was possible for TM atoms to react with AlB_2 to form TMB_2s following the order of Zr, Hf, Ti, Ta, and Nb. Because ZrB_2 had the largest lattice constant in TMB_2s,

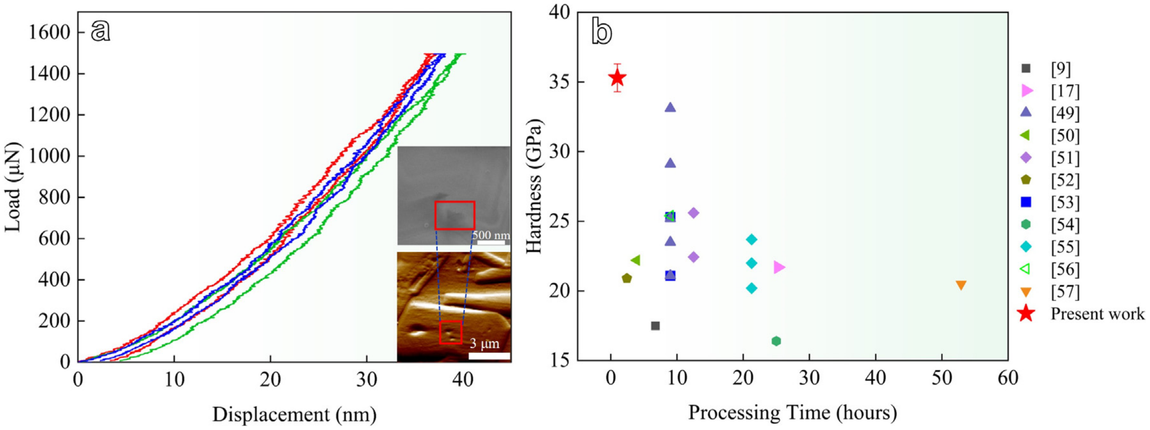

Fig. 6. (a) Nanoindentation load-displacement curves of as-synthesized MMB_2 powders; (b) The comparison of the hardness of MMB_2 obtained by different preparation methods. The processing time in the horizontal coordinate is the time taken to obtain the $(HfTaZrNbTi)B_2$ single-phase product, excluding the subsequent densification into bulk.

the other metal atoms could enter the ZrB_2 lattice and generate numerous MMB_2 nuclei.

3.3. Mechanical properties of *MMB_2* microcrystals

The typical load–displacement curves obtained for the benchmark TMB_2 and MMB_2 samples are shown in Fig. 6(a) and Fig. S4, respectively. We observed that the three curves of the MMB_2 sample matched well in Fig. 6(a), which verified the experimental results. The insets in Fig. 6(a) presents the shape of the indentation, and the calculated average hardness values at an indentation load of 1500 μN are listed in Table S2, according to the obtained results. Among the benchmark borides, TiB_2 had the highest hardness, reaching 37.2 GPa, with the hardness values of HfB_2, NbB_2, ZrB_2, and TaB_2 decreasing in turn. By contrast, the hardness of the obtained MMB_2 was 35.3 GPa, which was 20.3 % higher than the calculated one according to the rule of mixtures. The increased hardness was attributed to mass disorder and solid solution hardening, which was mainly caused by the metallic sublattice populated by the different transition metals [48,49]. Because of the increased configuration entropy, it is found that MMB_2 had a higher anti-oxidation ability than TMB_2s at high temperatures [26,27]. Therefore, it can be used for high-temperature applications due to its improved oxidation resistance and similar mechanical properties as TiB_2.

We also compared the hardness and synthesized time of the MMB_2 with those reported ones in the literature and the MMB_2 obtained in this work had significantly higher hardness values than those reported in the literature as shown in Fig. 6(b) [9,17,49-57]. Meanwhile, the prepared efficiency of MMB_2 is enhanced significantly. Although other MMB_2 with different components have been reported, which still require a long time to form a single-phase structure and will not help to the rapid development of high entropy ceramic systems (Fig. S5).

A major concern associated with these mentioned fabrication methods involves the long mechanical pre-treatment time required to induce the formation of a single-phase product. As a result, the corresponding overall processing time will be significantly extended. In addition, the extremely abrasive character of TMB_2 will cause the related powders to be contaminated by the milling media, which can result in crucial issues. However, in this work, an alternative, more efficient approach was developed using aluminum molten as the medium processing method. This system consisted of in-situ reaction and nucleation growth processes using high entropy products in the Al melt. This finding served as a breakthrough in understanding the intrinsic properties of high-entropy boride ceramics and may broaden potential applications.

To elucidate the effect of Al doping on the mechanical properties of $(HfTaZrNbTi)B_2$, first-principles calculations were performed, and a total of three MMB_2 models with different Al contents were calculated, which were denoted as MMB_2, MMB_2–1, and MMB_2–2. Table S3 presents the number of atoms for each constituent element in the calculation of each MMB_2 model. The atomic percentages of the transition metal atoms had nearly equal atomic ratios, while the percentage values of Al atoms were 0, 4.94 %, and 14.81 %. The calculated results are plotted in Fig. 7, and the calculated elastic constant values for all the binary and MMB_2 compounds assessed in this work are shown in Table S4. The G/B and ν results were also similar to the data reported in previous studies, with the values of G/B and ν serving as the most widely used indicators to evaluate material brittleness and ductility [38,58-61]. Specifically, a material was considered ductile when $G/B < 0.57$ or $\nu > 0.26$; otherwise, the material was regarded as brittle. Gu reported that increasing VEC enhanced the filling of d-t_{2g} and d-e_g orbitals, leading to improved metallicity and ductility of IVB and VB borides [62].

The H, E, and G/B values of Al-containing $(HfTaZrNbTi)B_2$ are shown in Fig. 7(a, b, c), which underwent monotonic decrease as VEC decrease from MMB_2 (3.5) to MMB_2–1 (3.4) and MMB_2–2 (3.3). While the ν values in Fig. 7(d) showed a clearly increased trend from 0.17 at VEC = 3.5 to 0.18 at VEC = 3.4 then 0.201 at VEC = 3.2. Thus, with increasing Al content in $(HfTaZrNbTi)B_2$, the Young's modulus and hardness values decreased, yet the toughness was improved.

In order to measure the fracture toughness (K_{IC}) of the synthesized Al-containing MMB_2, the extracted powders were further sintered into a bulk by arc-melting. The fracture toughness was tested by the indentation method with an applied load of 1 kg, held for 10 s according to Ref. [63]. The SEM images and EDS compositional maps of the Al-containing MMB_2 bulk are shown in Fig. 8(a) and (a1), respectively. It can be seen that, except for a distinct Ta-enriched area (corresponding to the Zr-depleted zone), the distribution of the remaining elements is almost uniform in the whole area.

The Vickers indentation method was employed to measure the fracture toughness of the Al-containing MMB_2 bulk. The fracture toughness of the MMB_2 bulk was determined to be 3.44 ± 0.25 MPa $m^{1/2}$, which is larger than that of conventional metal boride. The fracture toughness of ZrB_2 and HfB_2 reported in the literature is generally less than 3.2 MPa $m^{1/2}$ [64,65].

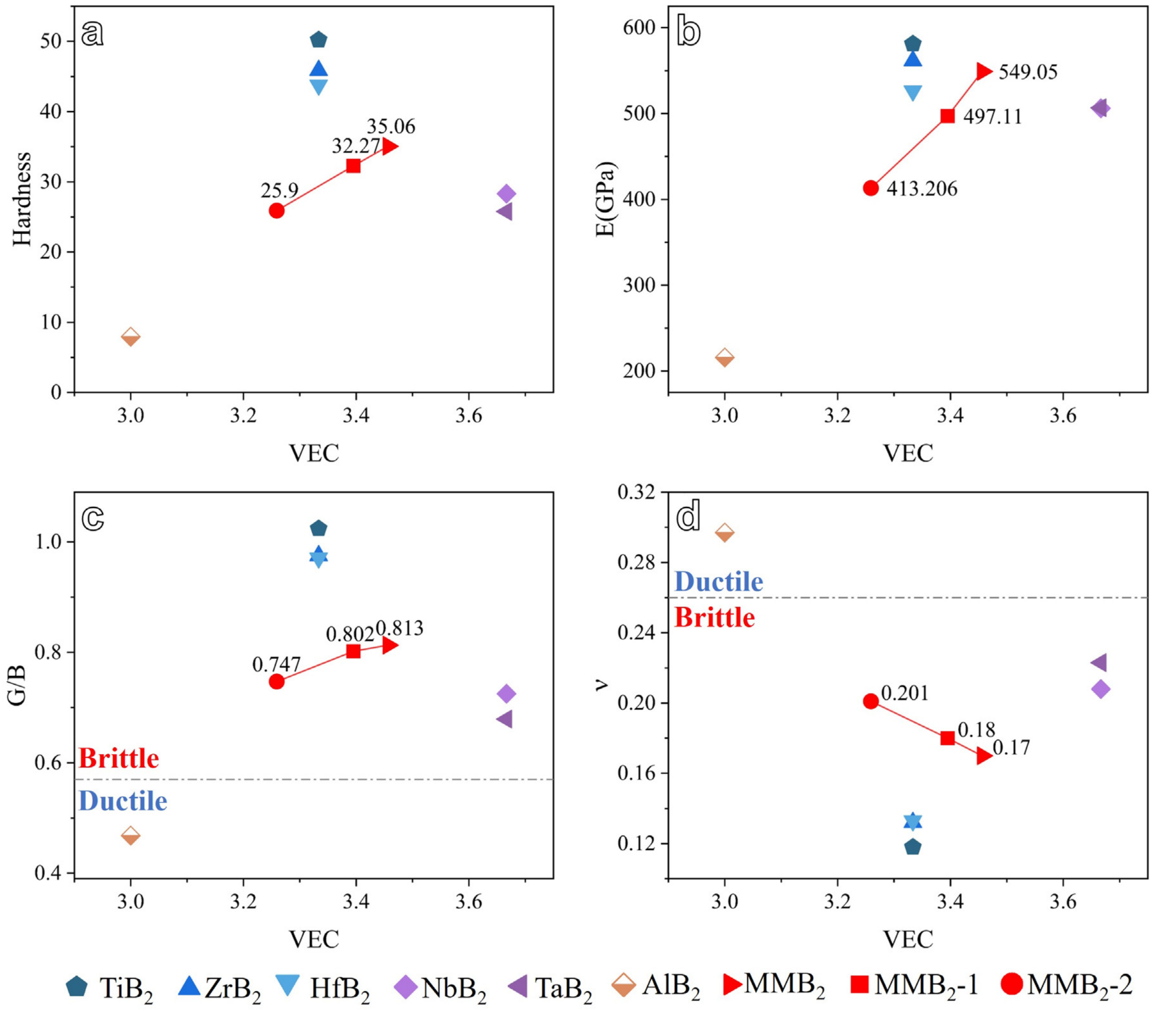

Fig. 7. The variation trends of (a) hardness *H*, (b) Young's modulus *E*, (c) Pugh's ratio *G*/*B* and (d) Poisson's ratio *ν* for the six TMB_2s compounds and Al-containing MMB_2 as VEC changes.

Fig. 8(b) shows the propagation behavior of the cracks, revealing that radial cracks extend from the corners of the surface indentation. The crack exhibits a typical zigzag propagation path during extension as shown in Fig. 8(b1). The deflection increases during the crack propagation, consuming the energy required for crack advancement and thereby enhancing toughness. In contrast, in traditional single-phase ceramic structures, radial cracks from indentations typically follow a straight propagation path.

Although the effect of element segregation on the toughness is not yet fully revealed, the synthesized Al-containing MMB_2 has been shown to exhibit high hardness, toughness and oxidation resistance demonstrated by first-principles calculations and experiments. The excellent performance of Al-containing MMB_2 makes them show great application potentials in the thermal structural components and thermal protection systems of aerospace devices that need to withstand extreme environments such as high temperature and pressure, high temperature oxidation, and high-speed airflow.

Designing ceramic materials with both high hardness and high toughness remains a challenge due to their trade-off relationship for traditional ceramics. However, this work provided a simple method via tuning VEC by introducing Al atoms into MMB_2s, making it possible to design ceramic materials with superior comprehensive performance.

Table 3
Details of samples and oxidation tests, heating rates (°C/min), peak oxidation temperature (T_p) and the weight change after oxidation.

Samples	Heating rates (°C/min)	T_p (°C/min)	Weight change after oxidation (%)
MMB_2–10	10	650	158
MMB_2–15	15	653	157
MMB_2–20	20	657	157

3.4. Oxidation test

To investigate the oxidation behaviors of the as-synthesized Al-containing multi-component boride powders, the TG-DSC test was conducted at different heating rates and the results are shown in Fig. 9(a, b). In these figures, only the interested region, that is, the range of temperature comprising the oxidation peak and corresponding mass gain, respectively at different rates, is shown. The details of the oxidized powder samples are listed in Table 3, the last digit of their names refers to the heating rate. The DSC curves of the samples show a typical trend with increasing heating rate, an increase in the maximum of heat flow, and a shift of the weight gain curves to higher temperatures. This is because the sample cannot take up the heat so fast and any phase transition

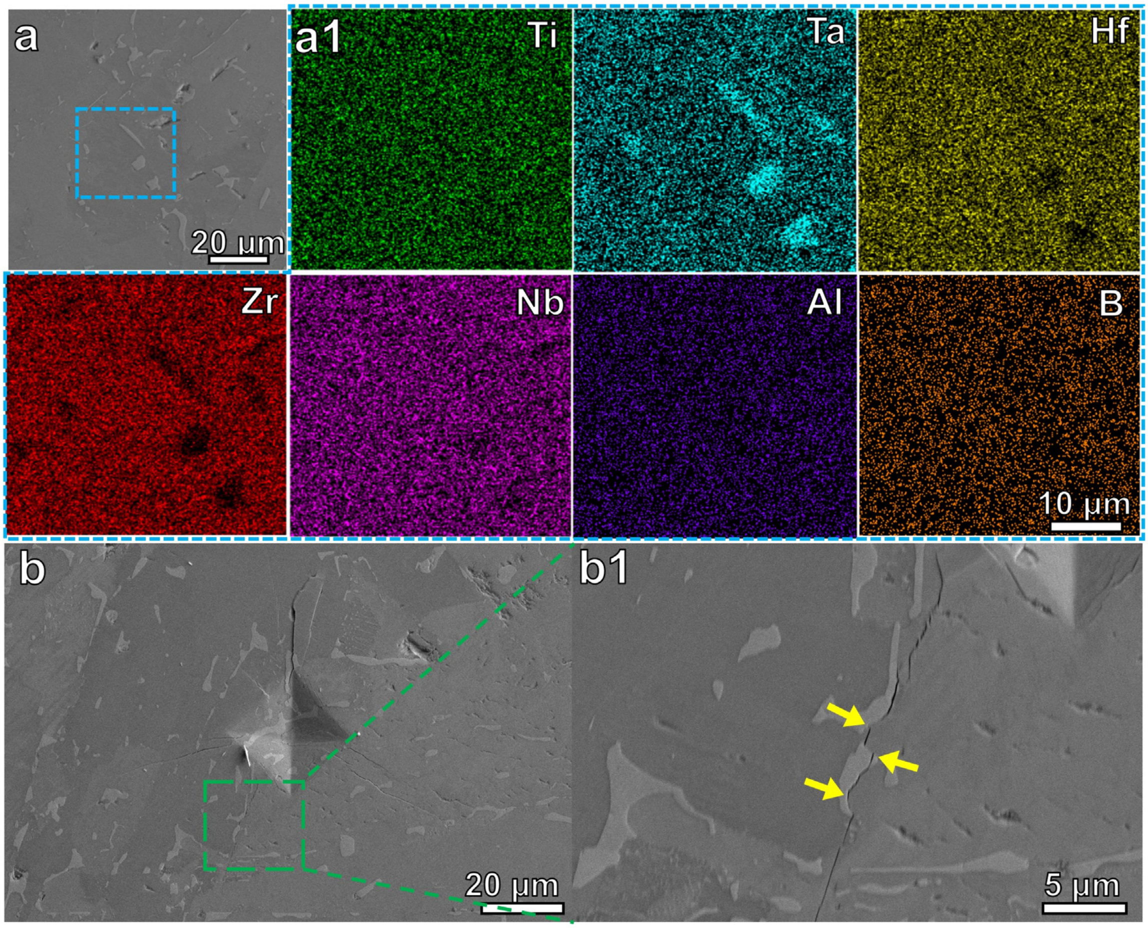

Fig. 8. (a) SEM image of as-synthesized Al-containing MMB_2 bulk; (a1) the corresponding EDS compositional maps; (b, b1) SEM image of Vickers indentation initiated by a load of 9.8 N on the well-polished surface of MMB_2.

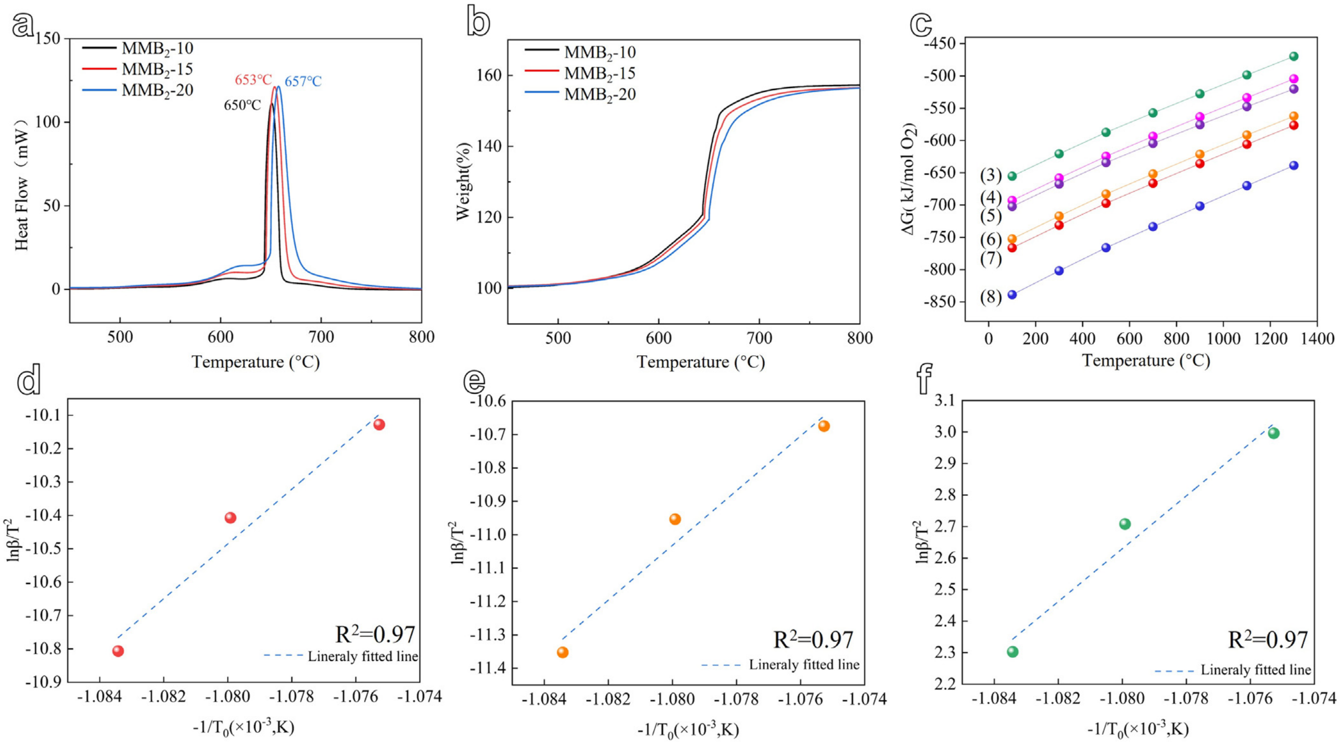

Fig. 9. (a, b) DSC curves and TG curves of MMB_2 at RT ~800 °C and different heating rates; (c) Thermodynamic analysis of the Reactions (3–8); (d–f) Plots of Kissinger model, Flynn-Wall-Ozama model and Starink model respectively.

Table 4
Activation energy of oxidation of the MMB_2 sample calculated using different methods.

Samples	Kissinger Model		FWO model		Starink model	
	E (kJ/mol)	R^2	E (kJ/mol)	R^2	E (kJ/mol)	R^2
MMB_2	681	0.97	732	0.97	682	0.97

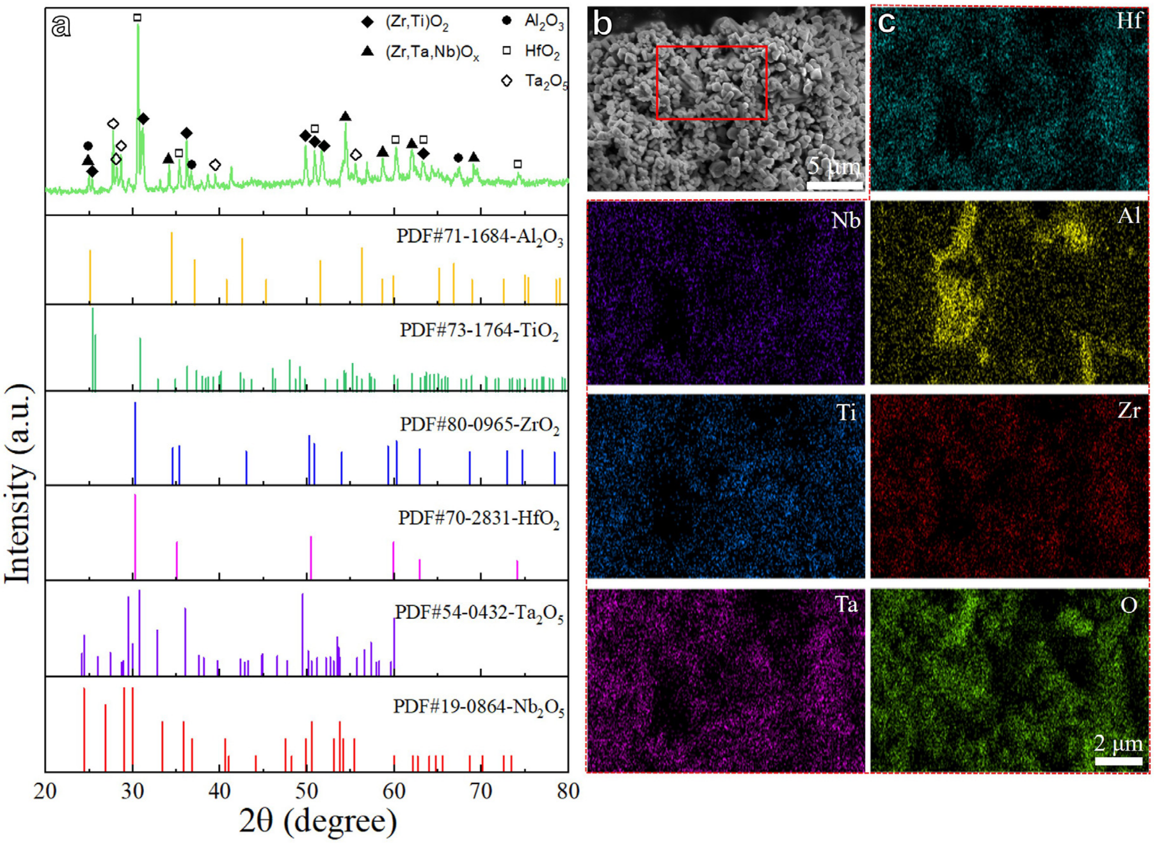

Fig. 10. Characterization results of the MMB_2 after TG-DSC oxidation test: (a) XRD pattern; (b) SEM image; (c) The corresponding EDS mapping analysis in the rectangular box of (b).

or reaction (oxidation in this case) shifts to a higher temperature [66]. Furthermore, the reaction is exothermic, and its peak oxidation temperature (T_p) occurs at 650 °C, 653 °C and 657 °C, at heating rates of 10 °C/min, 15 °C/min and 20 °C/min respectively, as shown in Fig. 9(a). Fig. 9(b) exhibits the weight change curves of MMB_2 as a function of oxidation temperature. The MMB_2 particles undergo a process of weight gain during oxidation and follow a characteristic "S-shaped" curve, showing an increased gain rate with increasing temperature at the early stage and a slower gain rate at the later stage. The oxidation of $(HfTaZrNbTi)B_2$ results in a mass gain of ~ 58 % which indicates that the oxidation process is complete and have been converted to the corresponding oxides.

The oxidation processes were further explored based on thermodynamic analysis (Fig. 9(b)) to in-depth understand the oxidation mechanism of MMB_2. It is theoretically that the oxidation of MMB_2 can be regarded as the combined oxidation of constituent TMB_2 components, and the element composition has a significant effect on the oxidation resistance of the material. Accordingly, the possible oxide reactions are described as Reactions (3)–(8), and the relationships between the standard Gibbs free energy changes (ΔG) of the above reactions and the temperature (T) are shown in Fig. 9(c). The Reactions (3–7) are the main oxidation reactions of transition metal borides HfB_2, ZrB_2, TiB_2, NbB_2 and TaB_2. The oxidation process of AlB_2 is also described by Reaction (8). It can be observed that the Reactions (3–7) can be spontaneous below 1400 °C. However, the Reaction (8) is more likely to proceed spontaneously than the Reaction (3–7) because it is more negative which demonstrates that the preferential formation of Al_2O_3 will occur. The preformed protective Al_2O_3 oxide layer could slow down oxidation by acting as a diffusion barrier.

$$2/5TiB_2(s) + O_2(g) = 2/5TiO_2(s) + 2/5\,B_2O_3(l) \tag{3}$$

$$2/5\,ZrB_2(s) + O_2(g) = 2/5ZrO_2(s) + 2/5\,B_2O_3(l) \tag{4}$$

$$2/5\,HfB_2(s) + O_2(g) = 2/5HfO_2(s) + 2/5\,B_2O_3(l) \tag{5}$$

$$4/11\,NbB_2(s) + O_2(g) = 2/11Nb_2O_5(s) + 4/11\,B_2O_3(l) \tag{6}$$

$$4/11\,TaB_2(s) + O_2(g) = 2/11Ta_2O_5(s) + 4/11\,B_2O_3(l) \tag{7}$$

$$4/9\,AlB_2(s) + O_2(g) = 2/9Al_2O_3(s) + 4/9\,B_2O_3(l) \tag{8}$$

Based on the peak oxidation temperature shown in the DSC curves, the oxidation activation energy of the MMB_2 powders can be calculated using different integral isoconversional methods [67–69], such as Kissinger method, Flynn-Wall-Ozama (FWO model)

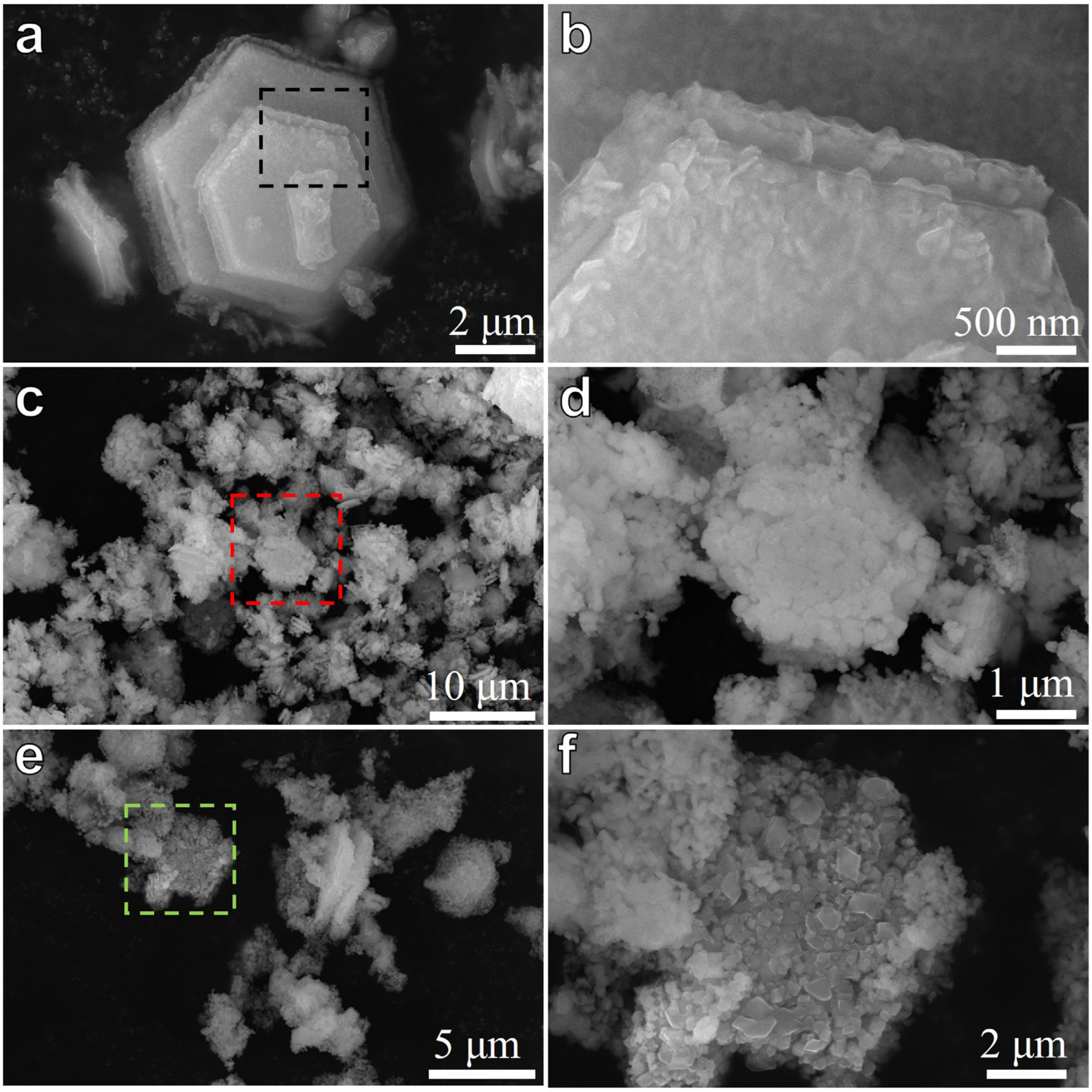

Fig. 11. SEM images of the as-synthesized MMB_2 after isothermal oxidation at different temperature: (a, b) 600 °C for 2 h; (c, d) 650 °C for 2 h; (e, f) 800 °C for 2 h.

and Starink method. The oxidation activation energy E can be obtained from each fitted line and the corresponding correlation coefficient, R^2 (which determines the goodness of the fit) are reported in Fig. 9(d-f) and Table 4. The calculated results showed that the oxidation activation energy for $(HfTaZrNbTi)B_2$ was found to be 681 kJ/mol, 732 kJ/mol and 682 kJ/mol obtained using different methods, respectively.

Up to now, there is rarely report about the isothermal oxidation behavior of high entropy borides, most of the previous studies mainly focus on transition metal di-borides. It has been reported that ZrB_2 and HfB_2 exhibit excellent oxidation resistance among all transition metal boride based ultrahigh temperature ceramics at elevated temperatures due to the protective nature of the corresponding oxide layers [70]. For example, Hassan et al. synthesized ZrB_2-SiC powder and studied its oxidation behavior [66]. The average activation energy of ZrB_2-SiC powder oxidation was calculated to be 593 kJ/mol. In addition, the oxidation resistance of ZrB_2 and ZrB_2-SiC powders was investigated by simultaneous thermal analysis technique in air [69]. The average activation energy for oxidation of ZrB_2 and in ZrB_2-SiC powder was obtained as 249 and 308 kJ/mol, respectively. Although the activation energy for oxidation may be affected by the prepared method of samples, nature and flow rate of gas utilized, etc., it is clear that the oxidation activation energy of as-synthesized MMB_2, is significantly higher than that of TMB_2 as previously reported. The increase in activation energy of MMB_2 is attributed to the superior oxidization resistance of possibly results from the sluggish diffusion of O_2 caused by the severe lattice distortion.

Fig. 10 presents the microstructure of the MMB_2 after isothermal oxidation tests to investigate the high-temperature oxidation mechanism. The phase composition of the powders after oxidation tests was detected by XRD (Fig. 10(a)). It is obviously that the diffraction peak positions are multiple overlaps, indicating that the oxide products are not a simple mixture of single Me_xO_y (Ta_2O_5, Nb_2O_5, TiO_2, HfO_2 and ZrO_2) phases. The XRD diffraction peaks can be divided into three sets: one set of diffraction peaks can be indexed to complex oxides including $(Zr, Hf)O_2$ and $(Zr, Ta, Nb)O_x$, another set of diffraction peaks can be indexed to Me_xO_y:Ta_2O_5 and HfO_2 and the last one can be indexed to Al_2O_3. Fig. 10(b, c) present SEM images and the corresponding EDS mapping analysis of the samples after isothermal oxidation tests. EDS mapping analysis MMB_2 (Fig. 10(c)) indicates that the distribution of five metal elements (Ti, Zr, Hf, Nb, Ta) is highly uniform without any segregation or aggregation in all areas for the oxidation products at 1200 °C. However, it's interesting to note that the Al element segregation is found in oxidation products. This phenomenon is in good agreement with XRD results that oxidation products are consisted of the major TM_xO_y phase and the minor Al_2O_3 phase. Combined with the thermodynamics analysis, the preferential formation of Al_2O_3 would enhance the oxidation resistance by slowing down the oxidation rate [25,71]. The oxidation of MMB_2 particles mainly depends on the diffusion of oxygen and the possible formation of an interlayer between oxide and boride, which acts as an effective diffusion barrier for oxygen.

In addition, we studied the morphology changes of MMB_2 after isothermal oxidation tests at different temperature. Fig. 11(a, b) and (c, d) presents the SEM images of the oxidized products at 600 °C and 650 °C, respectively, and the particles retain their original shape and size. They begin to disintegrate after oxidation at 800 °C as shown in Fig. 11(e, f), but basically maintain their original shape, indicating that MMB_2 has good oxidation stability.

Based on the above analysis, the synthesized MMB_2 microcrystals display superior oxidation activation energy and structure stability. The enhanced oxidation resistance is mainly attributed to the formation of a protective Al-containing oxide and the severe lattice distortion which both cause the sluggish diffusion of O_2. The formation of the Al_2O_3 oxide is caused by the preferential oxidation of Al elements. Besides, after oxidation, the particles of MMB_2 maintain their original shape with only a few cracks, therefore demonstrating greater structural stability.

4. Conclusion

In summary, we have proposed a high-efficiency strategy for preparing MMB_2 particles in a molten aluminum medium using the spontaneous in-situ reaction between dissolved transitional metal atoms and boron atoms for the first time. The prepared Al-containing $(TiZrHfNbTa)B_2$ microcrystals had a homogeneous composition with a hexagonal AlB_2 structure. The formation process of the as-synthesized MMB_2 ceramic including in-situ reaction and growth mechanism was also proposed. In addition, the hardness of the obtained MMB_2 in this work was 35.3 GPa, which was much higher than the rule of mixture estimations data reported in the literature. Furthermore, combined with the First-principles calculation results, we found that the toughness of multi-component boride microcrystals is obviously enhanced by the trace-doped Al elements. Moreover, the fabricated MMB_2 microcrystals have superior oxidation activation energy. The enhanced oxidation resistance is mainly attributed to the formation of a protective Al_2O_3 oxide caused by the preferential oxidation of Al elements which lead to sluggish diffusion of O_2. Besides, after oxidation, the particles maintain their original shape with only a few cracks, showing greater structural stability. Altogether, our work offers a facile high-efficiency preparation strategy for designing multi-component boride microcrystals with superior comprehensive performance including ultra-hardness, intrinsically improved toughness and oxidation resistance. This finding not only enriches the knowledge regarding the categories of multi-component ceramics, but also accelerates the exploration of high-performance ceramics to achieve unexplored properties.

Author contributions

J. Nie conceived the original idea; Y. Fan synthesized the alloys and ceramic particles and carried out the microstructural characterization and nanoindentation; J. Nie, Y. Fan, Z. Ding and S. Liu analyzed the crystal growth and strengthening mechanism; J. Nie, Y. Fan and Y. Zhao wrote the paper; all authors contributed to the discussion of the results.

Additional information

All data is available in the main text or the supplementary materials. Correspondence and requests for materials should be addressed to niejinfeng@njust.edu.cn, sidaliu@xjtu.edu.cn, yhzhao@njust.edu.cn

Declaration of competing interests

The authors declare that they have no known competing financial interests or personal relationships that could have appeared to influence the work reported in this paper.

Acknowledgements

This work was financially supported by the National Natural Science Foundation of China (Nos. 52271033 and 52071179), the Key program of National Natural Science Foundation of China (No. 51931003), Natural Science Foundation of Jiangsu Province, China (No. BK20221493), Jiangsu Province Leading Edge Technology Basic Research Major Project (No. BK20222014), Foundation of "Qinglan Project" for Colleges and Universities in Jiangsu Province.

Supplementary materials

Supplementary material associated with this article can be found, in the online version, at doi:10.1016/j.jmst.2024.02.074.

References

[1] H. Chen, X. Zou, Inorg. Chem. Front. 7 (2020) 2248–2264.
[2] W.G. Fahrenholtz, G.E. Hilmas, I.G. Talmy, J.A. Zaykoski, J. Am. Ceram. Soc. 90 (2007) 1347–1364.
[3] B.R. Golla, A. Mukhopadhyay, B. Basu, S.K. Thimmappa, Prog. Mater. Sci. 111 (2020) 100651.
[4] B. Basu, V. Parameswaran, H. Wang, S.-H. Lee, Ceram. Int. 41 (2015) 8468–8474.
[5] D.W. Lipke, S.V. Ushakov, A. Navrotsky, W.P. Hoffman, Corros. Sci. 80 (2014) 402–407.
[6] S. Akrami, P. Edalati, M. Fuji, K. Edalati, Mater. Sci. Eng. R 146 (2021) 100644.
[7] D. Demirskyi, T.S. Suzuki, K. Yoshimi, O. Vasylkiv, J. Ceram. Soc. Jpn. 128 (2020) 977–980.
[8] D. Liu, Y. Chu, S. Jing, B. Ye, X. Zhou, J. Am. Ceram. Soc. 101 (2018) 4899–4904.
[9] J. Gild, Y. Zhang, T. Harrington, S. Jiang, T. Hu, M.C. Quinn, W.M. Mellor, N. Zhou, K. Vecchio, J. Luo, Sci. Rep. 6 (2016) 37946.
[10] D. Demirskyi, T. Nishimura, K. Yoshimi, O. Vasylkiv, Scr. Mater. 225 (2023) 115170.
[11] P. Zhang, C. Cheng, B. Liu, W. Xie, X. Zhu, J. Zhang, Q. Fu, Ceram. Int. 48 (2022) 12608–12624.
[12] F.-Z. Dai, Y. Sun, B. Wen, H. Xiang, Y. Zhou, J. Mater. Sci. Technol. 72 (2021) 8–15.
[13] Z. Wen, H. Meng, S. Jiang, Z. Tang, Y. Liu, Y. Chu, Sci. China Mater. 66 (2023) 3213–3222.
[14] O.F. Dippo, N. Mesgarzadeh, T.J. Harrington, G.D. Schrader, K.S. Vecchio, Sci. Rep. 10 (2020) 21288.
[15] M. Gaboardi, F. Monteverde, F. Saraga, G. Aquilanti, L. Feng, W. Fahrenholtz, G. Hilmas, Acta Mater. 239 (2022) 118294.
[16] G. Tallarita, R. Licheri, S. Garroni, S. Barbarossa, R. Orrù, G. Cao, J. Eur. Ceram. Soc. 40 (2020) 942–952.
[17] Y. Zhang, Z.-B. Jiang, S.-K. Sun, W.-M. Guo, Q.-S. Chen, J.-X. Qiu, K. Plucknett, H.-T. Lin, J. Eur. Ceram. Soc. 39 (2019) 3920–3924.
[18] D. Liu, H. Liu, S. Ning, B. Ye, Y. Chu, J. Am. Ceram. Soc. 102 (2019) 7071–7076.
[19] D. Liu, T. Wen, B. Ye, Y. Chu, Scr. Mater. 167 (2019) 110–114.
[20] D. Liu, H. Liu, S. Ning, Y. Chu, J. Adv. Ceram. 9 (2020) 339–348.
[21] Y. Yang, J. Bi, X. Gao, K. Sun, L. Qiao, G. Liang, H. Wang, Ceram. Int. 49 (2023) 19523–19527.
[22] Y. Zhou, H. Xiang, Z. Feng, Z. Li, J. Mater. Sci. Technol 31 (2015) 285–294.
[23] Z. Cao, N. Jin, J. Ye, X. Du, Y. Liu, RSC Adv. 10 (2020) 36295–36302.
[24] P. Zhang, X. Liu, A. Cai, Q. Du, X. Yuan, H. Wang, Y. Wu, S. Jiang, Z. Lu, Sci. China Mater. 64 (2021) 2037–2044.
[25] B. Bakhit, J. Palisaitis, J. Thornberg, J. Rosen, P.O.A. Persson, L. Hultman, I. Petrov, J.E. Greene, G. Greczynski, Acta Mater. 196 (2020) 677–689.
[26] L. Backman, J. Gild, J. Luo, E.J. Opila, Acta Mater. 197 (2020) 20–27.
[27] L. Backman, J. Gild, J. Luo, E.J. Opila, Acta Mater. 197 (2020) 81–90.
[28] Y. Yan, Y. Liao, K. Wang, Corros. Sci. 223 (2023) 111457.

[29] R. Guo, Z. Li, L. Li, Y. Liu, R. Zheng, C. Ma, J. Eur. Ceram. Soc. 42 (2022) 2127–2134.
[30] G. Kresse, D.P. Joubert, Phys. Rev. B 59 (1999) 1758–1775.
[31] M. Fuchs, M. Scheffler, Comput. Phys. Commun. 119 (1999) 67–98.
[32] J.P. Perdew, K. Burke, M. Ernzerhof, Phys. Rev. Lett. 77 (1996) 3865–3868.
[33] J.P. Perdew, Phys. B-Condens. Matter 172 (1991) 1–6.
[34] G.S. Priyanga, R. Rajeswarapalanichamy, K. Iyakutti, J. Rare Earths 33 (2015) 289–303.
[35] M. Lishi, D. Yonghua, L. Runyue, Structural, Phys. B-Condens. Matter 507 (2017) 147–155.
[36] R. Hill, Proc. Phys. Soc. A 65 (1952) 349.
[37] Y. Tian, B. Xu, Z. Zhao, Int. J. Refract. Hard Met. 33 (2012) 93–106.
[38] A.L. Ivanovskii, Int. J. Refract. Hard Met. 36 (2013) 179–182.
[39] C. Li, Y.Y. Wu, H. Li, X.F. Liu, Acta Mater. 59 (2011) 1058–1067.
[40] W. Sun, F. Dai, H. Xiang, J. Liu, Y. Zhou, J. Mater. Sci. Technol. 35 (2019) 584–590.
[41] C. Hu, J. Zou, Q. Huang, G. Zhang, S. Guo, Y. Sakka, J. Am. Ceram. Soc. 95 (2012) 85–88.
[42] M. Elwenspoek, J. Cryst. Growth. 78 (1986) 353–356.
[43] Y. Shiohara, A. Endo, Mater. Sci. Eng. R 19 (1997) 1–86.
[44] F. Meng, S.A. Morin, A. Forticaux, S. Jin, Acc. Chem. Res 46 (2013) 1616–1626.
[45] A. Takeuchi, A. Inoue, Mater. Trans. 46 (2005) 2817–2829.
[46] F.-Z. Dai, Y. Zhou, Comput. Mater. Sci 117 (2016) 266–269.
[47] P. Vajeeston, P. Ravindran, C. Ravi, R. Asokamani, Phys. Rev. B 63 (2001) 045115.
[48] Y.F. Ye, Q. Wang, J. Lu, C.T. Liu, Y. Yang, Mater. Today 19 (2016) 349–362.
[49] L. Feng, F. Monteverde, W.G. Fahrenholtz, G.E. Hilmas, Scr. Mater. 199 (2021) 113855.
[50] F. Monteverde, F. Saraga, M. Gaboardi, J.R. Plaisier, J. Eur. Ceram. Soc. 41 (2021) 6255–6266.
[51] J. Gu, J. Zou, S.-K. Sun, H. Wang, S.-Y. Yu, J. Zhang, W. Wang, Z. Fu, Sci. China Mater. 62 (2019) 1898–1909.
[52] M. Qin, J. Gild, H. Wang, T. Harrington, K.S. Vecchio, J. Luo, J. Eur. Ceram. Soc. 40 (2020) 4348–4353.
[53] L. Feng, W.G. Fahrenholtz, G.E. Hilmas, F. Monteverde, J. Eur. Ceram. Soc. 41 (2021) 92–100.
[54] Y. Zhang, S.-K. Sun, W. Zhang, Y. You, W.-M. Guo, Z.-W. Chen, J.-H. Yuan, H.-T. Lin, Ceram. Int. 46 (2020) 14299–14303.
[55] J.-X. Liu, X.-Q. Shen, Y. Wu, F. Li, Y. Liang, G.-J. Zhang, J. Adv. Ceram. 9 (2020) 503–510.
[56] L. Feng, W.G. Fahrenholtz, G.E. Hilmas, J. Eur. Ceram. Soc. 40 (2020) 3815–3823.
[57] J. Gild, A. Wright, K. Quiambao-Tomko, M. Qin, J.A. Tomko, M.S.B. Hoque, J.L. Braun, B. Bloomfield, D. Martinez, T. Harrington, K. Vecchio, P.E. Hopkins, J. Luo, Ceram. Int. 46 (2020) 6906–6913.
[58] T. Chihi, M. Reffas, M. Fatmi, A. Bouhemadou, B. Ghebouli, M.A. Ghebouli, Chin. J. Phys. 53 (2015) 150703.
[59] X. Wang, Y. Zhang, P.C. Liu, J. Yan, W. Mo, P. Zhang, X. Chen, RSC Adv. 6 (2016) 44561–44568.
[60] Y.H. Duan, Y. Sun, Z.Z. Guo, M.J. Peng, P.X. Zhu, J.H. He, Comput. Mater. Sci 51 (2012) 112–116.
[61] R.P. Thompson, W.J. Clegg, Curr. Opin. Solid State Mater. Sci. 22 (2018) 100–108.
[62] X. Gu, C. Liu, H. Guo, K. Zhang, C. Chen, Acta Mater. 207 (2021) 116685.
[63] A.G. Evans, E.A. Charles, J. Am. Ceram. Soc. 59 (1976) 371–372.
[64] E.W. Neuman, G.E. Hilmas, W.G. Fahrenholtz, Mater. Sci. Eng. A 670 (2016) 196–204.
[65] Z. Wang, X. Liu, B. Xu, Z. Wu, Int. J. Refract. Met. Hard Mater. 51 (2015) 130–136.
[66] R. Hassan, K. Balani, Corros. Sci. 177 (2020) 109024.
[67] S. Sarkar, P.K. Das, J. Therm. Anal. Calorim. 107 (2012) 1093–1103.
[68] Y. Hu, Z. Wang, X. Cheng, C. Ma, RSC Adv. 8 (2018) 22909–22916.
[69] F. Li, Y. Cao, J. Liu, H. Zhang, S. Zhang, Ceram. Int. 43 (2017) 7743–7750.
[70] W.G. Fahrenholtz, G.E. Hilmas, Int. Mater. Rev. 57 (2012) 61–72.
[71] J. Thörnberg, B. Bakhit, J. Palisaitis, N. Hellgren, L. Hultman, G. Greczynski, P.O.Å. Persson, I. Petrov, J. Rosen, Surf. Coat. Technol. 420 (2021) 127353.